ALMA observations of CH₃COCH₃ and the related species CH₃CHO, CH₃OH, and C₂H₅CN in line-rich molecular cores

Chuanshou Li¹, Sheng-Li Qin¹, Tie Liu², Xunchuan Liu², Xiaohu Li³, Li Chen¹, Hong-Li Liu¹, Fengwei Xu^{4,5}, Meizhu Liu⁶, Mengyao Tang⁷, Hongqiong Shi¹, Tianwei Zhang^{8,9}, and Yuefang Wu⁵

- School of Physics and Astronomy, Yunnan University, Kunming 650091, People's Republic of China e-mail: lichuanshou2021@163.com, qin@ynu.edu.cn
- ² Shanghai Astronomical Observatory, Chinese Academy of Sciences, 80 Nandan Road, Shanghai 200030, People's Republic of China
- e-mail: liutie@shao.ac.cn
- ³ Xinjiang Astronomical Observatory, Chinese Academy of Sciences, Urumqi 831399, China
- Kavli Institute for Astronomy and Astrophysics, Peking University, Beijing, 100871, People's Republic of China
- ⁵ Department of Astronomy, School of Physics, Peking University, Beijing, 100871, People's Republic of China
- ⁶ Center for Astrophysics, Guangzhou University, Guangzhou 510006, People's Republic of China
- Institute of Astrophysics, School of Physics and Electronic Science, Chuxiong Normal University, Chuxiong 675000, People's Republic of China
- I. Physikalisches Institut, Universität zu Köln, Zülpicher Straße 77, 50937 Köln, Germany
- ⁹ Research Center for Intelligent Computing Platforms, Zhejiang Laboratory, Hangzhou 311100, P.R.China

March 11, 2025

ABSTRACT

Context. Acetone (CH₃COCH₃) is a carbonyl-bearing complex organic molecule, yet interstellar observations of acetone remain limited. Studying the formation and distribution of CH₃COCH₃ in the interstellar medium can provide valuable insights into prebiotic chemistry and the evolution of interstellar molecules.

Aims. We explore the spatial distribution of CH_3COCH_3 and its correlation with the O-bearing molecules acetaldehyde (CH_3CHO) and methanol (CH_3OH), as well as the N-bearing molecule ethyl cyanide (C_2H_5CN), in massive protostellar clumps.

Methods. We observed 11 massive protostellar clumps using ALMA at 345 GHz, with an angular resolution of 0.7"-1.0". Spectral line transitions were identified using the eXtended CASA Line Analysis Software Suite. We constructed integrated intensity maps of CH₃COCH₃, CH₃CHO, CH₃OH, and C₂H₅CN and derived their rotation temperatures, column densities, and abundances under the assumption of local thermodynamic equilibrium.

Results. CH_3COCH_3 is detected in 16 line-rich cores from 9 massive protostellar clumps: 12 high-mass cores (core mass >8 M_{\odot}), 3 intermediate-mass cores (2–8 M_{\odot}), and 1 low-mass core ($<2\,M_{\odot}$). CH_3CHO and CH_3OH are also detected in all 16 cores, while C_2H_5CN is detected in 15. The integrated intensity maps reveal similar spatial distributions for CH_3COCH_3 , CH_3CHO , CH_3OH , and C_2H_5CN . The line emission peaks of all four molecules coincide with the continuum emission peaks in regions without ultra-compact $H_{\rm II}$ regions. Significant correlations are observed in the abundances of these molecules, which also exhibit similar average temperatures.

Conclusions. Our observational results, supported by chemical models, suggest that CH₃COCH₃, CH₃CHO, and CH₃OH originate from the same gas. The observed temperatures and abundances of CH₃COCH₃ are consistent with model predictions involving grain surface chemistry.

Key words. Astrochemistry – line: identification – ISM: molecules – ISM: abundance – star: formation

1. Introduction

Carbonyl-bearing complex organic molecules (COMs) are considered potential precursors of complex biomolecules (Bennett & Kaiser 2007; Jalbout 2008; Halfen et al. 2011; Frigge et al. 2018). The formation mechanisms of carbonyl-bearing COMs have garnered significant interest in astrochemistry and astrobiology (Bennett & Kaiser 2007; Bennett et al. 2007; Frigge et al. 2018). Acetone (CH₃COCH₃) is a representative carbonyl-bearing COM; it is characterized by its symmetric structure centered on the C=O group. It was the first COM containing ten atoms discovered in the interstellar medium (ISM; Combes et al. 1987; Snyder et al. 2002; Andrade et al. 2014). Recent advances in radio telescope technology have enabled the de-

tection of CH₃COCH₃ in high- (Friedel et al. 2005; Isokoski et al. 2013; Peng et al. 2013; Feng et al. 2015; Rong et al. 2016; Zou & Widicus Weaver 2017; Palau et al. 2017; Suzuki et al. 2018; Csengeri et al. 2019; Peng et al. 2022; Mininni et al. 2023), intermediate- (Palau et al. 2011; Fuente et al. 2014), and low-mass star-forming regions (Jørgensen et al. 2011; Imai et al. 2016; Lykke et al. 2017; van Gelder et al. 2020; Martín-Doménech et al. 2021).

Interferometric observations of the Orion-KL region have shown that the spatial distribution of CH₃COCH₃ is primarily concentrated in the hot core, rather than in the compact ridge, resembling that of complex cyanides (Friedel & Snyder 2008; Peng et al. 2013). This seems to imply a potential chemical relationship between the formation of CH₃COCH₃ and N-bearing

species. Although CH₃COCH₃ has been detected in various astronomical sources, its study has largely been confined to individual targets observed with interferometers or to small samples observed using single-dish telescopes. Hence, its physical and chemical properties remain poorly understood. Given that COMs are typically localized in compact regions within star-forming environments (Lykke et al. 2017; Qin et al. 2022), comprehensive interferometric studies targeting CH₃COCH₃ and chemically associated molecules across a larger sample with a similar angular resolution and spectral setup are essential.

We conducted observations of 11 massive protostellar clumps using Band 7 of the Atacama Large Millimeter/submillimeter Array (ALMA). These data serve as a pilot project for the ALMA Three-millimeter Observations of Massive Star-Forming Regions (ATOMS) survey and are a subsample of ATOMS (Liu et al. 2020; Xu et al. 2024). The 11 clumps have masses ranging from $(1-22) \times 10^3$ M_{\odot} and fall between the early stages of massive star formation and the HII region phase, with L/M ratios ranging from 12 to 80 (Xu et al. 2024). Eight of the clumps enshroud ultra-compact (UC) HII regions, as indicated by the presence of associated H40 α emission (Qin et al. 2022; Zhang et al. 2023). The primary goal of this study is to investigate the physical and chemical properties of the CH₃COCH₃ molecule by comparing it with the O-bearing molecules CH₃CHO and CH₃OH, as well as the Nbearing molecule C₂H₅CN.

The observations and data reduction are described in Sect. 2. Section 3 presents the observational results, including the line identification, spatial distribution, and parameter calculations for CH₃COCH₃, CH₃CHO, CH₃OH, and C₂H₅CN. The chemical implications of these findings are discussed in Sect. 4, and the conclusions are summarized in Sect. 5.

2. Observations

The sample selection for the ALMA observations is described in detail by Xu et al. (2024) and Chen et al. (2024). The ALMA Band-7 data for 11 massive protoclusters were obtained between May 18 and May 20, 2018 (Project ID: 2017.1.00545.S; PI: Tie Liu), using 43 12-meter antennas in the C43-1 configuration, with baselines ranging from 15.0 to 313.7 meters. The Band-7 observations included four spectral windows (SPWs): 342.36-344.24 GHz (SPW 31), 344.25-346.09 GHz (SPW 29), 356.60–357.07 GHz (SPW 27), and 354.27–354.74 GHz (SPW 25). SPWs 27 and 25 provided a bandwidth of 469 MHz with a spectral resolution of 0.24 km s⁻¹, while SPWs 31 and 29 offered a bandwidth of 1875 MHz with a spectral resolution of 0.98 km s⁻¹. In this paper we present spectral line data from the broader SPWs, SPW 31 and SPW 29. The calibrators used for flux and bandpass calibration were J1427-4206, J1517-2422, and J1924-2914, while phase calibration was performed using J1524-5903, J1650-5044, and J1733-3722. Data calibration was carried out using Common Astronomy Software Applications (CASA; Mc-Mullin et al. 2007) version 5.1.15. The deconvolution was performed using the "hogbom" algorithm with a weighting parameter of "briggs," and the robust parameter was set to 0.5 to balance sensitivity and resolution. Continuum imaging and line cubes were generated with the TCLEAN task in CASA 5.3. The continuum images were constructed from line-free channels across four SPWs. Due to the rich spectral line features of the sample, fewer than 10% of the channels were available as line-free, resulting in relatively poor continuum sensitivity. Self-calibration was applied to improve the quality of the continuum images.

The self-calibration solutions derived from the continuum images were applied to the line cubes. Primary beam correction was applied using pblimit = 0.2. The final synthesized beam sizes for both the continuum images and line cubes range from 0.7 to 1.0 arcsec. The average sensitivity of the continuum images is ~ 1.2 mJy beam $^{-1}$, and the mean sensitivity of the line cubes is ~ 4.7 mJy beam $^{-1}$ per channel.

3. Results

3.1. Line identifications

A total of 145 dense cores were identified across the 11 clumps, and 28 cores from 9 clumps were classified as line-rich (Chen et al. 2024). Spectra were extracted from a single pixel at the continuum peak position of the dense core and averaged over the beam. In this work, we used the eXtended CASA Line Analysis Software Suite (XCLASS1; Möller et al. 2017) to identify spectral lines in the 28 line-rich cores. XCLASS accesses two molecular databases, the Cologne Database for Molecular Spectroscopy (CDMS²; Müller et al. 2001, 2005) and the Jet Propulsion Laboratory (JPL³; Pickett et al. 1998) catalogs. Under the assumption of local thermodynamic equilibrium (LTE), XCLASS solves the radiative transfer equation and generates synthetic spectra for specific molecular transitions, accounting for factors such as source size, beam filling factor, line profile, opacity, and blending. The primary parameters for fitting each molecule include source size (θ) , rotation temperature (T), column density (N), line width (ΔV), and velocity offset (V_{off}). In our study, the source size was taken as the deconvolved size of the continuum emission (see Table A.1), which was derived from 2D Gaussian fitting in CASA (Chen et al. 2024). As shown in Fig. 2, in some sources, the molecular line emissions appear more extended than the continuum emissions. This may lead to an underestimation of the source size, resulting in an overestimate of the fitted column densities. XCLASS also integrates with the model optimizer package, Modeling and Analysis Generic Interface for eXternal numerical codes (MAGIX; Möller et al. 2013). MAGIX optimizes the parameter solutions and provides error estimations using various algorithms. We obtained the final fitting parameters and error estimates for the molecules using the Markov chain Monte Carlo algorithm.

Transitions are considered to be detected if their line intensities exceed 3σ noise level and the observed line intensities at different frequencies are consistent with the XCLASS model predictions. Molecular lines of CH₃COCH₃ are identified in 16 of the 28 line-rich cores. Table A.1 lists the target source names, distances, core positions, deconvolved sizes, peak flux densities, integrated flux densities, core masses, and H₂ column densities of the continuum cores, based on values reported by Chen et al. (2024). The source-averaged H₂ column densities of the 16 cores are derived from the continuum flux using the following formula under the LTE assumption (Kauffmann et al. 2008):

$$N(H_2) = \frac{S_{\nu}\eta}{\mu m_H \Omega \kappa_{\nu} B_{\nu}(T)},$$
(1)

where S_{ν} is the integrated flux density, $\eta=100$ is the gas-to-dust mass ratio (Lis et al. 1991; Hasegawa et al. 1992), $\mu=2.8$ is the mean molecular weight of the gas (Kauffmann et al. 2008), m_H is the mass of the hydrogen atom, $\kappa_{870\mu m}=1.89$ cm² g⁻¹

https://xclass.astro.uni-koeln.de

² http://cdms.de

³ http:///spec.jpl.nasa.gov

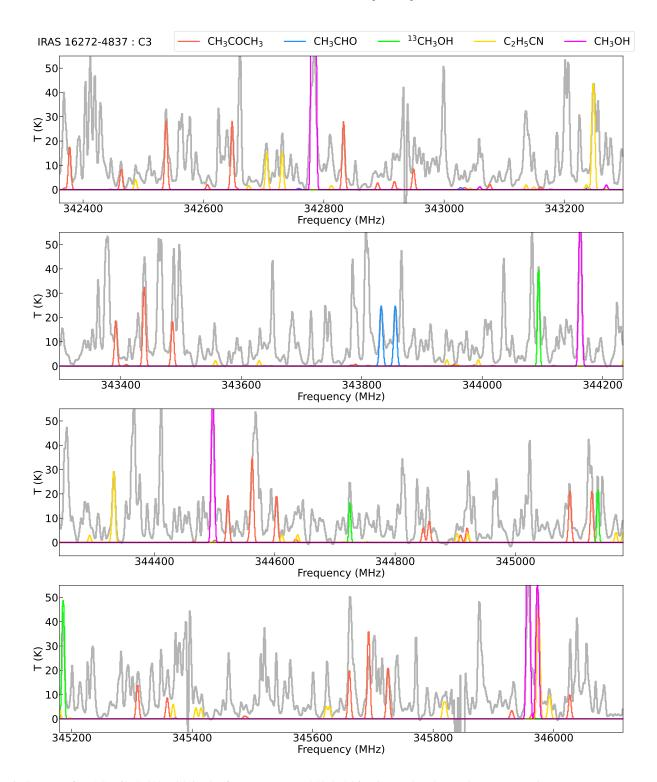


Fig. 1. Spectra of IRAS 16272-4837 C3 in the frequency range 342.4–346.1 GHz. The observed spectra are shown as gray curves, and the XCLASS-modeled spectra as colored curves. Spectra of other sources are presented in Fig. B.1.

is the dust mass absorption coefficient (Ossenkopf & Henning 1994), Ω is the solid angle subtended by the source, and $B_{\nu}(T)$ is the Planck function at dust temperature T (T is taken from Chen et al. 2024, and it is assumed to be equal to the gas temperature of CH₃OCHO). The 16 line-rich cores are classified into 12 high-mass line-rich cores (H, >8 M_{\odot}), 4 intermediate-mass line-rich cores (I, 2–8 M_{\odot}), and 1 low-mass line-rich core (L, <2 M_{\odot}) according to core mass. Line transitions of CH₃CHO

and CH₃OH are also detected in all 16 cores, while C₂H₅CN transitions are detected in 15 cores (excluding IRAS 16060 C2). Due to the optical thickness and blending of certain CH₃OH lines (see Appendix C), we fit the isotopolog ¹³CH₃OH as an alternative in the 16 cores. Figure 1 shows sample spectra toward IRAS 16272-4837 C3, with modeled molecular spectra for CH₃COCH₃, CH₃CHO, CH₃OH, ¹³CH₃OH, and C₂H₅CN overlaid. Additional spectra are presented in Fig. B.1. CH₃COCH₃,

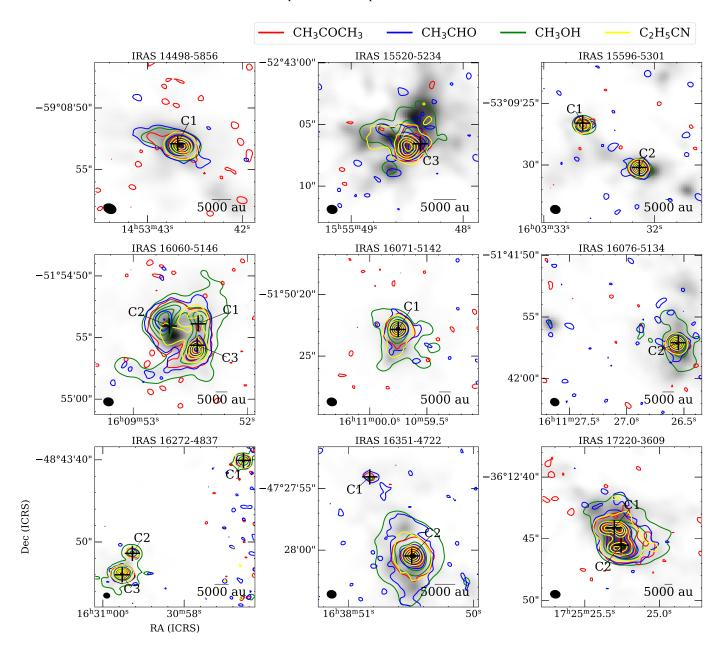


Fig. 2. Continuum emission in gray scale at 870 μ m overlaid with the integrated intensities of CH₃COCH₃, CH₃CHO, CH₃OH, and C₂H₅CN in nine high-mass star-forming regions. Colored contours represent the integrated intensities of each molecule. Contour levels are stepped by 10% of the peak values, with the outermost levels as follows: 4% for I14498, 6% for I15520, 10% for I15596, 1.3% for I16060, 1.3% for I16071, 5% for I16076, 1% for I16272, 0.8% for I16351, and 1.8% for I17220. Line-rich cores are named according to Li et al. (2024). The cross symbols mark the peak positions of the continuum emissions. The synthesized beam sizes are shown in the lower left, and scale bars are in the lower right.

¹³CH₃OH, and C₂H₅CN exhibit multiple transition lines, while CH₃CHO displays two transition lines in each core. Table C.1 lists the parameters of the CH₃COCH₃, CH₃CHO, CH₃OH, ¹³CH₃OH, and C₂H₅CN transitions. The upper level energy ranges of molecular transitions are 93−485 K for CH₃COCH₃, 227−459 K for CH₃OH, 36−144 K for ¹³CH₃OH, and 64−441 K for C₂H₅CN. CH₃CHO exhibits only two line transitions, with the same upper level energy of 166 K. We assumed that the fitting temperature of CH₃CHO is equal to the excitation temperature of CH₃COCH₃, as CH₃CHO is considered a precursor to CH₃COCH₃ (Garrod et al. 2022). The vibrational contributions of CH₃COCH₃, CH₃CHO, and ¹³CH₃OH are already included in the partition function, while the partition function of C₂H₅CN only considers the contribution from the ground state

in the XCLASS fitting. The vibrational correction factor (f_{vib}) can be given as (Tsuji 1966)

$$f_{vib} = \prod_{i} \frac{1}{1 - e^{-h\nu_i/kT}}, \qquad (2)$$

where h is Planck's constant, k is Boltzmann's constant, v_i is the vibrational frequency of mode i (Heise et al. 1981), and T is the temperature. The column densities of C_2H_5CN have been corrected by the f_{vib} .

3.2. Spatial distribution

We generated integrated intensity maps of CH₃COCH₃ at 342485 MHz, CH₃CHO at 343779 MHz, CH₃OH at 342730

MHz, and C₂H₅CN at 343195 MHz toward nine massive protostellar regions, as shown in Fig. 2. The spatial distributions of CH₃COCH₃ exhibit similarities with those of the O-bearing molecules CH₃CHO and CH₃OH, as well as the N-bearing molecule C₂H₅CN. The line emission peaks of these molecules coincide with the continuum peaks in most regions. The exceptions occur in I15520 C3, I16060 C1, C2 and C3, and I17220 C1 and C2, where the line emission peaks are offset from the continuum peaks. Intense UC H_{II} regions traced by the H40 α lines are found in I15520, I16060, and I17220 (Qin et al. 2022; Zhang et al. 2023), and the observed line offsets are likely influenced by UC H_{II} regions. Peng et al. (2013) reported that the distribution of CH₃COCH₃ in Orion-KL is similar to those of N-bearing molecules, but significantly different from those of complex Obearing molecules. However, in our larger sample, CH₃COCH₃ was found to be associated with the spatial distribution of both O- and N-bearing molecules. The resolved linear scale reported by Peng et al. (2013) is approximately 500 au, whereas the resolved linear scales of our samples exceed 2000 au. Future higher angular resolution observations may be able to resolve the differences in the spatial distribution of these molecules as in Orion KL. Previous studies have found that CH₃COCH₃ can only be detected in regions where C₂H₅CN is detected (Friedel & Snyder 2008; Peng et al. 2013). Nonetheless, I16060 C2 provides a counterexample, as C₂H₅CN is not detected in I16060 C2 (see Table A.2). The UC H_{II} region of I16060 is significantly stronger compared to I15520 and I17220 (Zhang et al. 2023), which may be linked to the absence of C_2H_5CN .

3.3. Rotation temperatures, column densities, and abundances

The rotation temperatures of CH_3COCH_3 and C_2H_5CN , as well as the column densities of CH_3COCH_3 , CH_3CHO , and C_2H_5CN in 16 line-rich cores are summarized in Table A.2. Since two transitions of CH_3CHO have the same upper energy level, the rotation temperature was fixed to that of CH_3COCH_3 and the column density was subsequently derived. The rotation temperature of CH_3OH was assumed to be the same as that of $^{13}CH_3OH$. The column densities of CH_3OH in 15 cores were taken from Li et al. (2024), which were calculated from the ^{12}C / ^{13}C ratios based on the column densities of $^{13}CH_3OH$. The ratios of ^{12}C / ^{13}C follow (Yan et al. 2019)

$$^{12}\text{C}/^{13}\text{C} = (5.08 \pm 1.10)\text{R}_{GC} + (11.86 \pm 6.60),$$
 (3)

where R_{GC} (in kpc) represents the distance from the Galactic Center (Liu et al. 2020). I17220 C2 is a CH₃COCH₃ core that is not compiled in Li et al. (2024), and the column density of CH₃OH was derived from a column density of ¹³CH₃OH of $(2.0\pm0.2)\times10^{17}$ cm⁻², using a 12 C / 13 C ratio of 18, computed by Eq. (3). The rotation temperature and column density of CH₃OH are presented in Table A.3. From Tables A.2 and A.3, the rotation temperatures range from 92 to 163 K for CH₃COCH₃, 95 to 250 K for C_2H_5CN , and 52 to 159 K for CH_3OH . The column densities span from 10^{15} to 10^{17} cm⁻² for CH_3COCH_3 and C_2H_5CN , 10^{14} to 10^{16} cm⁻² for CH_3CHO , and 10^{17} to 10^{19} cm⁻² for CH₃OH. In general, the column densities of the four molecules in the H cores are 1 to 2 orders of magnitude higher than those in the I and L cores. The fractional abundance of a given molecule relative to H_2 is expressed as $f_{H_2} = N/N(H_2)$, where N represents the column density of specific molecule and N (H₂) denotes the column density of molecular hydrogen. Tables A.2 and A.3 also show the abundances of four molecules relative to H₂. The molecules CH₃COCH₃ and C₂H₅CN exhibit comparable abundances, ranging from 10^{-9} to 10^{-7} . The abundance of CH₃CHO is found to be within the range 10^{-9} to 10^{-8} , while CH₃OH is approximately three orders of magnitude more abundant than the other molecules, with values ranging from 10^{-6} to 10^{-5} . The average abundances of the four molecules are $(6.2\pm1.3)\times10^{-8}$ for CH₃COCH₃, $(1.6\pm0.4)\times10^{-8}$ for CH₃CHO, $(9.0\pm1.7)\times10^{-6}$ for CH₃OH, and $(7.5\pm1.9)\times10^{-8}$ for C₂H₅CN. In clump I16351, the H core (C2) and L core (C1) residing in the same gas environment exhibit the highest and lowest CH₃COCH₃ abundances.

A comparison of the abundances of CH₃COCH₃, CH₃CHO, CH₃OH, and C₂H₅CN relative to H₂ in 16 line-rich cores is presented in Fig. 3. The correlation coefficients of CH₃COCH₃ with CH₃CHO, CH₃OH, and C₂H₅CN are 0.90, 0.61, and 0.91, respectively. CH₃COCH₃ exhibits a significant correlation (P<0.05) with CH₃OH and highly significant correlations (P<0.001) with CH₃CHO and C₂H₅CN. Abundance correlations between CH₃COCH₃ and C₂H₅CN, as well as between CH₃COCH₃ and CH₃OH, were also reported by Suzuki et al. (2018) in six high-mass star-forming regions, with correlation coefficients of 0.54 and 0.60, respectively. Figure 4 further compares the rotation temperatures of CH₃COCH₃, CH₃OH, and C₂H₅CN, showing no significant correlations in temperatures among these molecules. This indicates that the abundance correlations of these molecules are not affected by temperature. The average temperatures of the three molecules are 129±6 K for CH₃COCH₃, 119±9 K for CH₃OH, and 141±11 K for C₂H₅CN. Considering the errors, the average temperatures of the three molecules are comparable.

4. Discussion

4.1. Comparison of the physical parameters of CH₃COCH₃ in different sources

The rotation temperatures, column densities, and abundances of CH₃COCH₃ derived from our observations have been compared with those reported in high-, intermediate-, and low-mass starforming regions. The mean rotation temperature of CH₃COCH₃ in the H cores from our study is 134 K, the average column density is 4.2×10^{16} cm⁻², and the mean abundance is $7.5 \times$ 10⁻⁸. These values align with those found in high-mass starforming regions (Friedel et al. 2005; Peng et al. 2013; Rong et al. 2016; Csengeri et al. 2019; Peng et al. 2022). In the I cores, the mean column density of CH₃COCH₃ is 7.9×10^{15} cm⁻², which is comparable to that observed in intermediate-mass starforming regions (Jørgensen et al. 2011; Fuente et al. 2014). For the L cores, the CH₃COCH₃ column density of 1.6×10^{15} cm⁻² lies between values reported for low-mass protostars, including IRAS 16293-2422 ($\sim 10^{16} \text{ cm}^{-2}$; Lykke et al. 2017) and IRAS 19347+0727 ($\sim 10^{14} \text{ cm}^{-2}$; Imai et al. 2016). These comparisons suggest that the CH₃COCH₃ emitting gas in the H, I, and L cores may have similar physical and chemical conditions as those of high-, intermediate-, and low-mass star formation regions, respectively.

4.2. Chemistry

CH₃COCH₃, CH₃CHO, CH₃OH, and C₂H₅CN are simultaneously detected in 16 line-rich cores from our observations (except for C₂H₅CN in I16060 C2). The four molecules have also been commonly reported in other hot cores (Feng et al. 2015; Mininni et al. 2023; Fuente et al. 2014) and hot corinos (van Gelder et al. 2020). Moreover, CH₃COCH₃, CH₃CHO, and

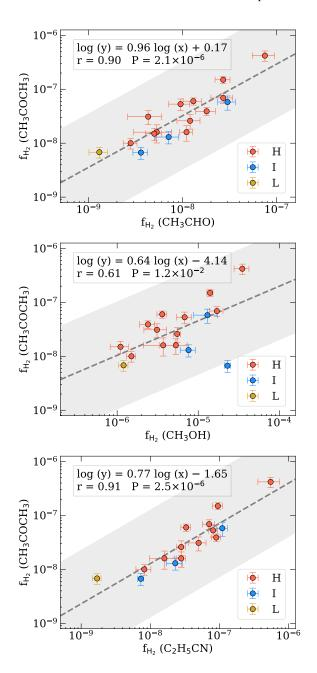


Fig. 3. Abundances of CH₃COCH₃, CH₃CHO, CH₃OH, and C₂H₅CN relative to H₂. Colored circles denote different types of cores: H (high-mass line-rich cores), I (intermediate-mass line-rich cores), and L (low-mass line-rich cores). The bars represent the 1σ errors estimated by MAGIX. Dashed lines represent linear least-squares fits to the data. The shaded regions indicate an order of magnitude scatter. Fitting results, Pearson correlation coefficients (r), and significance levels (P) are displayed in the upper left.

CH₃OH have been demonstrated to be chemically linked. On the grain surface, CH₃COCH₃ and CH₃OH share a common precursor, the methyl radical (CH₃), through the following reactions (Garrod et al. 2008; Suzuki et al. 2018):

$$CH_3 + OH \longrightarrow CH_3OH,$$
 (4)

$$CH_3 + CH_3CO \longrightarrow CH_3COCH_3.$$
 (5)

Article number, page 6 of 27

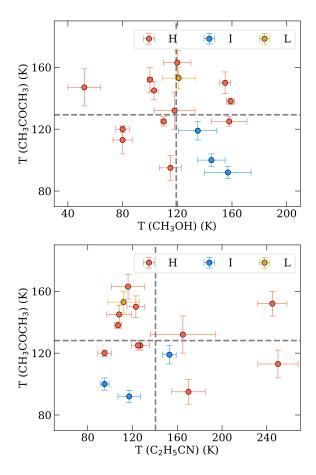


Fig. 4. Comparison of the rotation temperatures of CH₃COCH₃, CH₃OH, and C₂H₅CN. Colored circles denote different core types: H (high-mass line-rich cores), I (intermediate-mass line-rich cores), and L (low-mass line-rich cores). The bars represent the 1σ errors estimated by MAGIX. Dashed lines indicate the mean temperatures for each molecule.

Additionally, CH₃CHO acts as a precursor to CH₃COCH₃ via grain surface reactions (Garrod et al. 2022):

$$CH_3CHO + CH_2 \longrightarrow CH_3COCH_3,$$
 (6)

where CH₃CHO can be efficiently regenerated in the gas phase through the reaction of O with C₂H₅ (Garrod et al. 2022). In our observations, the morphological similarities, colocated line peaks at continuum sources, and abundance correlations among CH₃COCH₃, CH₃CHO, and CH₃OH provide further evidence that these molecules are chemically related and likely form on grain surfaces. Garrod et al. (2022) predicted the abundance of CH₃COCH₃ in the hot cores using reaction (6). The model employed three warm-up timescales: 5×10^4 years (fast), $2 \times$ 10^5 years (medium), and 1×10^6 years (slow). The predicted CH₃COCH₃ abundances for these timescales are 6.4×10^{-9} , 7.0 \times 10⁻⁹, and 1.4 \times 10⁻⁸, respectively. The average abundance of CH_3COCH_3 is $(6.2\pm1.3)\times10^{-8}$, which is comparable to the slow timescale model prediction. However, no chemical models suggest a direct association between CH₃COCH₃ and C₂H₅CN. It is possible that these two molecules coexist within similar physical environments without being chemically related.

5. Conclusions

We have presented a study of CH₃COCH₃ toward 11 massive protocluster clumps using ALMA Band-7 observations and analyzed the correlations among CH₃COCH₃, CH₃CHO, CH₃OH, and C₂H₅CN. Our main findings are as follows:

- CH₃COCH₃, CH₃CHO, and CH₃OH lines were detected in 16 line-rich cores, while C₂H₅CN lines were detected in 15 line-rich cores, across 9 of the 11 massive protocluster clumps considered.
- 2. Integrated intensity maps from the nine massive protocluster clumps reveal that the spatial distribution of CH₃COCH₃ is similar to that of the O-bearing molecules CH₃CHO and CH₃OH, as well as the N-bearing molecule C₂H₅CN.
- 3. The line peaks of the four molecules coincide with the continuum peaks in regions devoid of UC H_{II} regions. In the presence of UC H_{II} regions, the line peaks are offset from the continuum peaks.
- 4. CH₃COCH₃, CH₃CHO, CH₃OH, and C₂H₅CN exhibit significant abundance correlations, and CH₃COCH₃, CH₃OH, and C₂H₅CN have similar average temperatures.
- 5. The apparent spatial similarities and abundance correlations of CH₃COCH₃, CH₃CHO, and CH₃OH, combined with chemical models, suggest that these molecules originate from the same gas. The observed temperatures and abundances of CH₃COCH₃ are consistent with model predictions involving grain surface production.

Acknowledgements. This paper makes use of the following ALMA data: ADS/JAO.ALMA#2017.1.00545.S. ALMA is a partnership of ESO (representing its member states), NSF (USA), and NINS (Japan), together with NRC (Canada), MOST and ASIAA (Taiwan), and KASI (Republic of Korea), in cooperation with the Republic of Chile. The Joint ALMA Observatory is operated by ESO, AUI/NRAO, and NAOJ. This work has been supported by National Key R&D Program of China (No. 2022YFA1603101), and by NSFC through the grants No. 12033005, No. 12073061, No. 12122307, and No. 12103045. S.-L. Qin thanks the Xinjiang Uygur Autonomous Region of China for their support through the Tianchi Program. H.-L. Liu is supported by Yunnan Fundamental Research Project (grant No. 202301AT070118). Tie Liu thanks the supports by the international partnership program of Chinese Academy of Sciences through grant No.114231KYSB20200009, and Shanghai Pujiang Program 20PJ1415500. XHL acknowledges the support by NSFC through grants no. 12473025. T.Zhang thanks the student's exchange program of the Collaborative Research Center 956, funded by the Deutsche Forschungsgemeinschaft (DFG). We would like to thank the anonymous referee for the valuable comments and suggestions, which helped improve the quality of the manuscript.

References

Andrade, D. P. P., de Barros, A. L. F., Ding, J., et al. 2014, MNRAS, 444, 3792 Bennett, C. J., Chen, S.-H., Sun, B.-J., Chang, A. H. H., & Kaiser, R. I. 2007, ApJ, 660, 1588 Bennett, C. J. & Kaiser, R. I. 2007, ApJ, 661, 899 Chen, L., Qin, S.-L., Liu, T., et al. 2024, ApJ, 962, 13 Combes, F., Gerin, M., Wootten, A., et al. 1987, A&A, 180, L13 Csengeri, T., Belloche, A., Bontemps, S., et al. 2019, A&A, 632, A57 Feng, S., Beuther, H., Henning, T., et al. 2015, A&A, 581, A71 Friedel, D. N. & Snyder, L. E. 2008, ApJ, 672, 962 Friedel, D. N., Snyder, L. E., Remijan, A. J., & Turner, B. E. 2005, ApJ, 632, Frigge, R., Zhu, C., Turner, A. M., et al. 2018, ApJ, 862, 84 Fuente, A., Cernicharo, J., Caselli, P., et al. 2014, A&A, 568, A65 Garrod, R. T., Jin, M., Matis, K. A., et al. 2022, ApJS, 259, 1 Garrod, R. T., Widicus Weaver, S. L., & Herbst, E. 2008, ApJ, 682, 283 Halfen, D. T., Ilyushin, V., & Ziurys, L. M. 2011, ApJ, 743, 60 Hasegawa, T. I., Herbst, E., & Leung, C. M. 1992, ApJS, 82, 167 Heise, H. M., Winther, F., & Lutz, H. 1981, Journal of Molecular Spectroscopy, Imai, M., Sakai, N., Oya, Y., et al. 2016, ApJ, 830, L37

Isokoski, K., Bottinelli, S., & van Dishoeck, E. F. 2013, A&A, 554, A100 Jalbout, A. F. 2008, Origins of Life and Evolution of the Biosphere, 38, 489

Jørgensen, J. K., Bourke, T. L., Nguyen Luong, Q., & Takakuwa, S. 2011, A&A, 534, A100 Kauffmann, J., Bertoldi, F., Bourke, T. L., Evans, N. J., I., & Lee, C. W. 2008, A&A, 487, 993 Li, C., Qin, S.-L., Liu, T., et al. 2024, MNRAS, 533, 1583 Lis, D. C., Carlstrom, J. E., & Keene, J. 1991, ApJ, 380, 429 Liu, T., Evans, N. J., Kim, K.-T., et al. 2020, MNRAS, 496, 2790 Lykke, J. M., Coutens, A., Jørgensen, J. K., et al. 2017, A&A, 597, A53 Martín-Doménech, R., Bergner, J. B., Öberg, K. I., et al. 2021, ApJ, 923, 155 McMullin, J. P., Waters, B., Schiebel, D., Young, W., & Golap, K. 2007, in Astronomical Society of the Pacific Conference Series, Vol. 376, Astronomical Data Analysis Software and Systems XVI, ed. R. A. Shaw, F. Hill, & D. J. Mininni, C., Beltrán, M. T., Colzi, L., et al. 2023, A&A, 677, A15 Möller, T., Bernst, I., Panoglou, D., et al. 2013, A&A, 549, A21 Möller, T., Endres, C., & Schilke, P. 2017, A&A, 598, A7 Müller, H. S. P., Schlöder, F., Stutzki, J., & Winnewisser, G. 2005, Journal of Molecular Structure, 742, 215 Müller, H. S. P., Thorwirth, S., Roth, D. A., & Winnewisser, G. 2001, A&A, 370, L49 Ossenkopf, V. & Henning, T. 1994, A&A, 291, 943 Palau, A., Fuente, A., Girart, J. M., et al. 2011, ApJ, 743, L32 Palau, A., Walsh, C., Sánchez-Monge, Á., et al. 2017, MNRAS, 467, 2723 Peng, T. C., Despois, D., Brouillet, N., et al. 2013, A&A, 554, A78 Peng, Y., Liu, T., Qin, S.-L., et al. 2022, MNRAS, 512, 4419 kett, H. M., Poynter, R. L., J. Quant. Spectr. Rad. Transf., 60, 883 et al. 1998, Pickett, H. Cohen, E. A., Qin, S.-L., Liu, T., Liu, X., et al. 2022, MNRAS, 511, 3463 Rong, J., Qin, S.-L., Zapata, L. A., et al. 2016, MNRAS, 455, 1428 Snyder, L. E., Lovas, F. J., Mehringer, D. M., et al. 2002, ApJ, 578, 245 Suzuki, T., Ohishi, M., Saito, M., et al. 2018, ApJS, 237, 3 Tsuji, T. 1966, PASJ, 18, 127 van Gelder, M. L., Tabone, B., Tychoniec, Ł., et al. 2020, A&A, 639, A87 Xu, F., Wang, K., Liu, T., et al. 2024, ApJS, 270, 9 Yan, Y. T., Zhang, J. S., Henkel, C., et al. 2019, ApJ, 877, 154 Zhang, C., Zhu, F.-Y., Liu, T., et al. 2023, MNRAS, 520, 3245 Zou, L. & Widicus Weaver, S. L. 2017, ApJ, 849, 139

Appendix A: Parameters of line-rich cores

Table A.1. Physical parameters of the continuum sources.

Region	Core	D (kpc)	R.A. (h:m:s)	Dec. (∘ : ' : '')	$\begin{array}{c} \theta_{\rm dec} \\ {\rm maj}(\prime\prime) \times {\rm min}(\prime\prime) \end{array}$	$\begin{array}{c} I_{peak} \\ (mJy \; beam^{-1}) \end{array}$	$S_{\nu} \\ (mJy)$	$M_{core} \ (M_{\bigodot})$	N (H ₂) (cm ⁻²)	Mass ^a Classification
IRAS 14498-5856	C1	3.2	14:53:42.7	-59:08:52.8	3.2×1.9	340±22	2830±200	21.4±2.9	$(2.1\pm0.2)\times10^{23}$	Н
IRAS 15520-5234	C3	2.7	15:55:48.4	-52:43:06.5	2.0×1.4	200±5	1128±35	6.1±0.7	$(1.8\pm0.1)\times10^{23}$	I
IRAS 15596-5301	C1 C2	10.1		-53:09:26.6 -53:09:30.3	1.3×0.8 2.2×0.9	55±4 166±9	160±16 799±54	12.3±3.3 55.4±20.7	$(7.0\pm1.8)\times10^{22}$ $(1.7\pm0.6)\times10^{23}$	H H
IRAS 16060-5146	C1 C2 C3	5.3	16:09:52.7	-51:54:53.8 -51:54:53.9 -51:54:55.6	2.2×1.2 1.6×1.1 1.6×1.2	843±48 1530±160 1220±100	5000±330 6520±810 5500±550	93.6±12.7 99.2±16.1 105.0±15	$(7.6\pm0.7)\times10^{23}$ $(1.2\pm0.2)\times10^{24}$ $(1.2\pm0.1)\times10^{24}$	Н Н Н
IRAS 16071-5142	C1	5.3	16:10:59.8	-51:50:23.1	1.8×1.0	849±107	3840±580	62.9±12.4	$(7.5\pm1.3)\times10^{23}$	Н
IRAS 16076-5134	C2	5.3	16:11:26.5	-51:41:57.4	2.3×1.5	160±11	1410±110	30.5±5	$(1.9\pm0.2)\times10^{23}$	Н
IRAS 16272-4837	C1 C2 C3	2.9	16:30:58.6	-48:43:40.1 -48:43:51.4 -48:43:54.0	1.0×0.8 1.2×0.6 0.8×0.8	212±8 252±14 1144±51	549±27 638±49 2560±160	3.3±0.4 4.0±0.8 14.0±1.7	$(2.9\pm0.2)\times10^{23}$ $(3.9\pm0.7)\times10^{23}$ $(1.6\pm0.1)\times10^{24}$	I I H
IRAS 16351-4722	C1 C2	3.0		-47:27:54.1 -47:28:00.8	0.8×0.6 2.2×1.9	113±3 320±45	220±9 3010±470	1.7±0.2 11.6±2.3	$(2.3\pm0.3)\times10^{23}$ $(1.9\pm0.3)\times10^{23}$	L H
IRAS 17220-3609	C1 C2	8.0		-36:12:44.1 -36:12:45.4	3.6×1.4 2.6×1.3	554±19 595±26			$(4.9\pm0.6)\times10^{23}$ $(6.6\pm0.4)\times10^{23}$	H H

Notes. The basic parameters for the dense cores are adopted from Chen et al. (2024) and Li et al. (2024). $^{\alpha}$ H = high-mass line-rich core (> 8 M_{\odot}), I = intermediate-mass line-rich core (2-8 M_{\odot}), L = low-mass line-rich core (< 2 M_{\odot}).

Table A.2. Physical parameters of CH₃COCH₃, CH₃CHO, and C₂H₅CN.

	,		CH ₃ COCH ₃	3		СН3СНО			C_2H_5CN	
Kegion	Core	T (K)	N (cm ⁻²)	$f_{ m H_2}$	T (K)	N (cm ⁻²)	$f_{ m H_2}$	T (K)	N (cm ⁻²)	f_{H_2}
IRAS 14498-5856	CI	152±8	$(3.4\pm1.0)\times10^{15}$	$(1.6\pm0.5)\times10^{-08}$	152±8	$(2.2\pm0.3)\times10^{15}$	$(1.1\pm0.2)\times10^{-08}$	245±13	$(5.8\pm0.7)\times10^{15}$	$(2.8\pm0.4)\times10^{-08}$
IRAS 15520-5234	C3	100±4	$(1.6\pm0.3)\times10^{15}$	$(8.9\pm1.7)\times10^{-09}$	100±4	$(6.5\pm1.1)\times10^{14}$	$(3.6\pm0.6)\times10^{-09}$	95±4	$(1.3\pm0.1)\times10^{15}$	$(7.3\pm0.7)\times10^{-09}$
IRAS 15596-5301	C1 C2	113±9 95±8	$(2.2\pm0.3)\times10^{15}$ $(2.6\pm0.3)\times10^{15}$	$(3.1\pm0.9)\times10^{-08}$ $(1.6\pm0.6)\times10^{-08}$	113±10 95±8	$(3.0\pm0.9)\times10^{14}$ $(8.8\pm2.0)\times10^{14}$	$(4.3\pm1.7)\times10^{-09}$ $(5.3\pm2.3)\times10^{-09}$	250±18 170±15	$(3.5\pm0.5)\times10^{15}$ $(2.6\pm0.5)\times10^{15}$	$(5.0\pm1.4)\times10^{-08}$ $(1.6\pm0.6)\times10^{-08}$
IRAS 16060-5146	333	120±2 147±12 150±7	$(7.6\pm1.5)\times10^{15}$ $(1.8\pm0.4)\times10^{16}$ $(7.0\pm0.8)\times10^{16}$	$(1.0\pm0.2)\times10^{-08}$ $(1.5\pm0.4)\times10^{-08}$ $(6.0\pm0.9)\times10^{-08}$	120±2 147±12 150±7	$(2.1\pm0.3)\times10^{15}$ $(6.0\pm0.9)\times10^{15}$ $(1.5\pm0.3)\times10^{16}$	$(2.8\pm0.5)\times10^{-09}$ $(5.0\pm1.0)\times10^{-09}$ $(1.3\pm0.3)\times10^{-08}$	95±6 123±8	$(6.2\pm1.4)\times10^{15}$ $(3.9\pm0.5)\times10^{16}$	(8.2±2.0)×10 ⁻⁰⁹ (3.3±0.5)×10 ⁻⁰⁸
IRAS 16071-5142	C1	138±2	$(5.2\pm0.6)\times10^{16}$	$(6.9\pm1.4)\times10^{-08}$	138±2	$(2.0\pm0.4)\times10^{16}$	$(2.7\pm0.7)\times10^{-08}$	107±3	$(5.4\pm0.6)\times10^{16}$	$(7.1\pm1.4)\times10^{-08}$
IRAS 16076-5134	C2	163±8	$163\pm 8 (1.0\pm 0.2)\times 10^{16}$	$(5.3\pm1.3)\times10^{-08}$	163±8	$(1.8\pm0.4)\times10^{15}$	$(9.5\pm2.4)\times10^{-09}$	116±15	$(1.5\pm0.1)\times10^{16}$	$(8.1\pm1.2)\times10^{-08}$
IRAS 16272-4837	3 23 23	119±6 92±4 145±6	$(1.7\pm0.5)\times10^{16}$ $(5.2\pm0.9)\times10^{15}$ $(2.3\pm0.3)\times10^{17}$	$(5.8\pm1.7)\times10^{-08}$ $(1.3\pm0.3)\times10^{-08}$ $(1.5\pm0.2)\times10^{-07}$	119±6 92±4 145±6	$(8.9\pm1.8)\times10^{15}$ $(2.8\pm0.6)\times10^{15}$ $(4.2\pm0.7)\times10^{16}$	$(3.0\pm0.6)\times10^{-08}$ $(7.1\pm2.0)\times10^{-09}$ $(2.7\pm0.5)\times10^{-08}$	153±6 117±10 108±11	$(3.4\pm0.6)\times10^{16}$ $(9.2\pm1.7)\times10^{15}$ $(1.5\pm0.2)\times10^{17}$	$(1.1\pm0.2)\times10^{-07}$ $(2.3\pm0.6)\times10^{-08}$ $(9.5\pm1.6)\times10^{-08}$
IRAS 16351-4722	C1 C2	153 ± 7 132 ± 12	$(1.6\pm0.3)\times10^{15}$ $(7.8\pm1.1)\times10^{16}$	$(6.8\pm1.5)\times10^{-09}$ $(4.2\pm0.9)\times10^{-07}$	153±7 132±12	$(3.0\pm0.6)\times10^{14}$ $(1.4\pm0.3)\times10^{16}$	$(1.3\pm0.3)\times10^{-09}$ $(7.5\pm2.0)\times10^{-08}$	112±14 165±29	$(4.1\pm0.4)\times10^{14}$ $(1.0\pm0.3)\times10^{17}$	$(1.7\pm0.2)\times10^{-09}$ $(5.5\pm1.9)\times10^{-07}$
IRAS 17220-3609	C1 C3	125±3 125±3	$(1.9\pm0.2)\times10^{16}$ $(1.7\pm0.5)\times10^{16}$	$(3.9\pm0.6)\times10^{-08}$ $(2.6\pm0.8)\times10^{-08}$	125±3 125±4	$(9.0\pm1.8)\times10^{15}$ $(8.0\pm2.1)\times10^{15}$	$(1.8\pm0.4)\times10^{-08}$ $(1.2\pm0.3)\times10^{-08}$	127±8 125±2	$(4.5\pm0.4)\times10^{16}$ $(1.8\pm0.3)\times10^{16}$	$(9.0\pm1.4)\times10^{-08}$ $(2.8\pm0.4)\times10^{-08}$

Notes. The rotation temperature of CH₃CHO is assumed to be equal to that of CH₃COCH₃. "···" indicates no molecular lines were detected.

Table A.3. Physical parameters of CH₃OH derived from ¹³CH₃OH.

		СН ₃ ОН			
Region	Core	T (K)	N (cm ⁻²)	f_{H_2}	
IRAS 14498-5856	C1	100±2	$(1.1\pm0.4)\times10^{18}~a$	$(5.3\pm2.0)\times10^{-06}$	
IRAS 15520-5234	C3	145±10	$(4.1\pm0.3)\times10^{18}~a$	$(2.3\pm2.0)\times10^{-05}$	
IRAS 15596-5301	C1 C2	80±7 115±8	$(2.2\pm0.4)\times10^{17} a$ $(6.1\pm1.5)\times10^{17} a$	$(3.1\pm9.6)\times10^{-06}$ $(3.7\pm1.6)\times10^{-06}$	
IRAS 16060-5146	C1 C2 C3	80±5 52±12 155±4	$(1.1\pm0.1)\times10^{18} a$ $(1.3\pm0.3)\times10^{18} a$ $(4.2\pm0.4)\times10^{18} a$	$(1.5\pm1.9)\times10^{-06}$ $(1.1\pm2.8)\times10^{-06}$ $(3.6\pm5.0)\times10^{-06}$	
IRAS 16071-5142	C1	159±3	$(1.3\pm0.1)\times10^{19} a$	$(1.7\pm3.2)\times10^{-05}$	
IRAS 16076-5134	C2	120±10	$(1.3\pm0.2)\times10^{18}~a$	$(6.8\pm1.4)\times10^{-06}$	
IRAS 16272-4837	C1 C2 C3	135±14 157±17 103±3	$(3.7\pm1.2)\times10^{18} a$ $(3.0\pm0.3)\times10^{18} a$ $(2.3\pm0.1)\times10^{19} a$	$(1.3\pm4.2)\times10^{-05}$ $(7.6\pm1.6)\times10^{-06}$ $(1.4\pm1.2)\times10^{-05}$	
IRAS 16351-4722	C1 C2	121±12 118±15	$(2.9\pm0.2)\times10^{17} a$ $(6.6\pm0.8)\times10^{18} a$	$(1.2\pm1.6)\times10^{-06}$ $(3.5\pm7.3)\times10^{-05}$	
IRAS 17220-3609	C1 C2	110±2 158±13	$(1.2\pm0.2)\times10^{18} a$ $(3.6\pm0.3)\times10^{18} b$	$(2.4\pm5.1)\times10^{-06}$ $(5.5\pm5.6)\times10^{-06}$	

Notes. The rotation temperature of CH₃OH is assumed to be equal to that of 13 CH₃OH. ^a Derived by Li et al. (2024). ^b Derived from a column density of 13 CH₃OH of (2.0±0.2)×10¹⁷ cm⁻², using a 12 C / 13 C ratio of 18.

Appendix B: Spectra of line-rich cores

The spectra of CH_3COCH_3 , CH_3CHO , CH_3OH , $^{13}CH_3OH$, and C_2H_5CN in the frequency range 342.4–346.1 GHz for the 16 line-rich cores are presented in Figs. 1 and B.1.

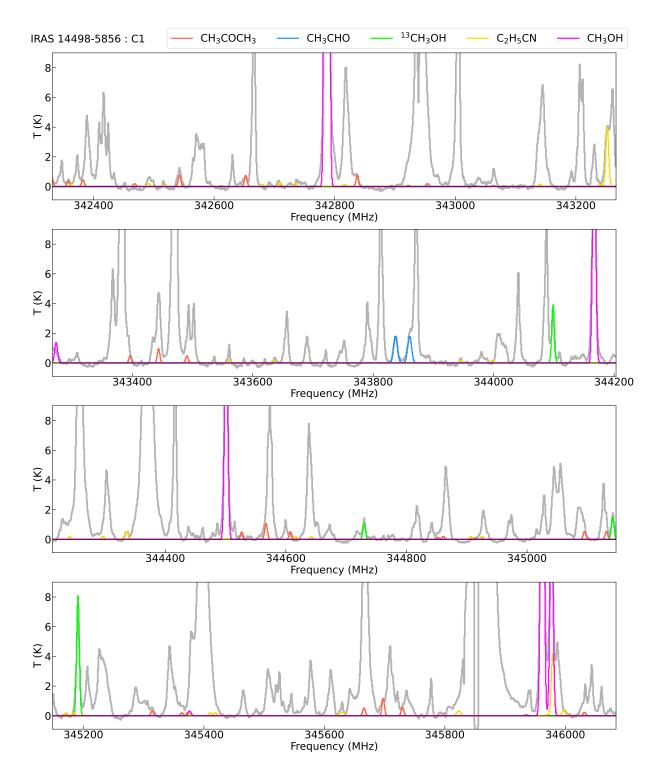


Fig. B.1. Same as Fig. 1, but for the other 15 line-rich cores.

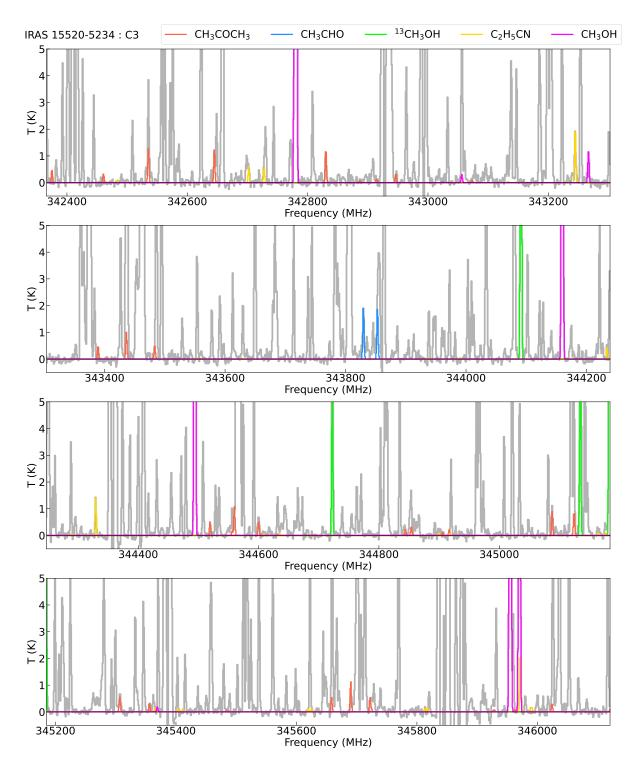


Fig. B.1. Continued.

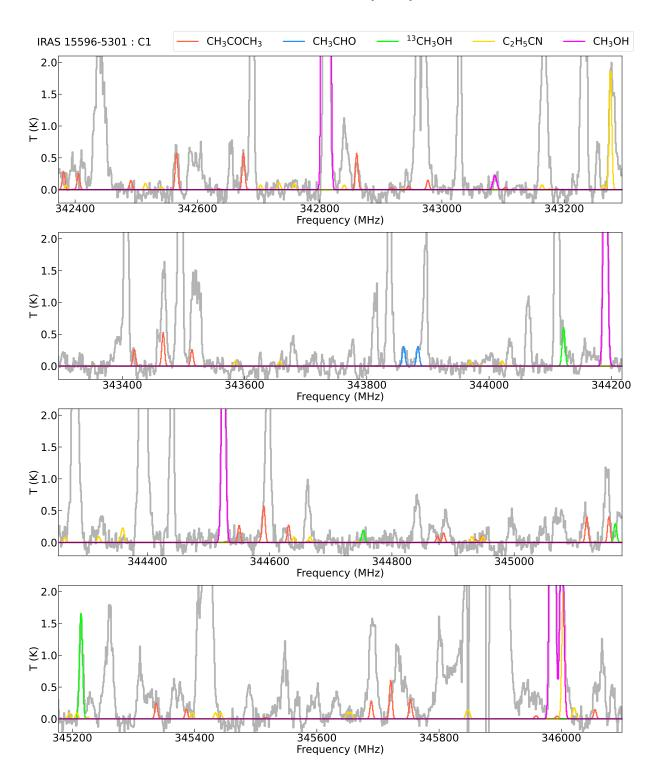


Fig. B.1. Continued.

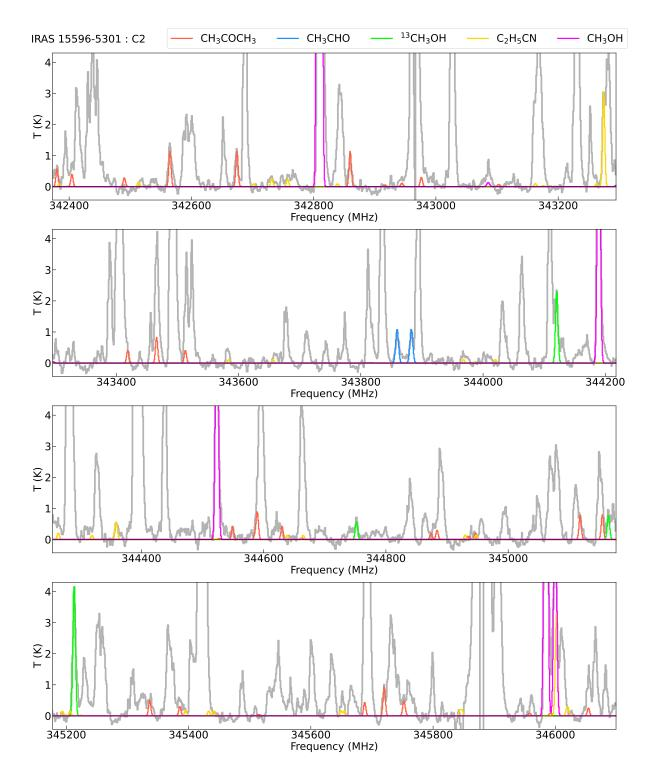


Fig. B.1. Continued.

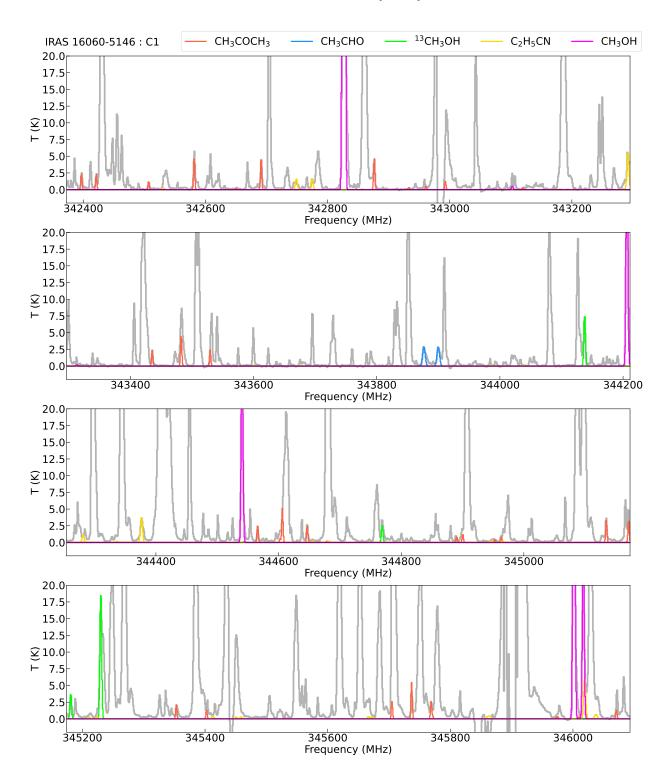


Fig. B.1. Continued.

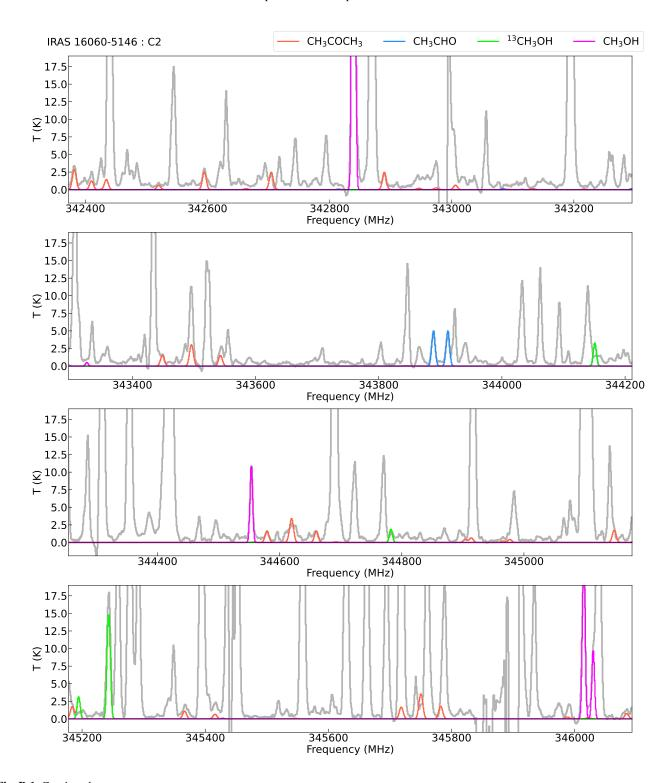


Fig. B.1. Continued.

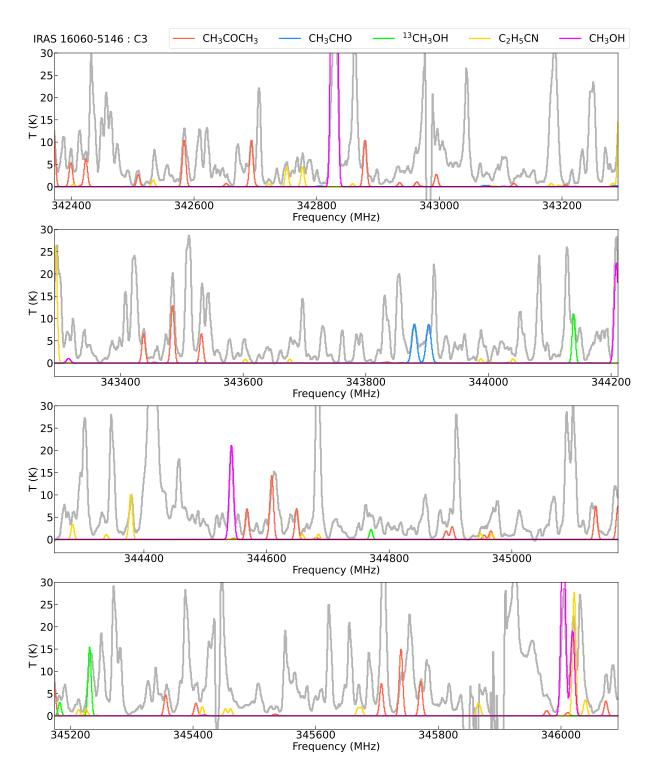


Fig. B.1. Continued.

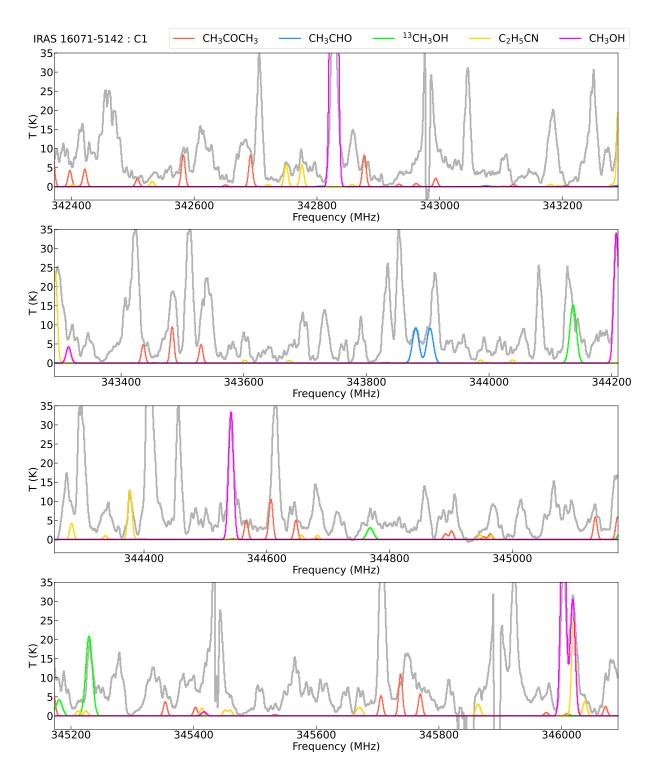


Fig. B.1. Continued.

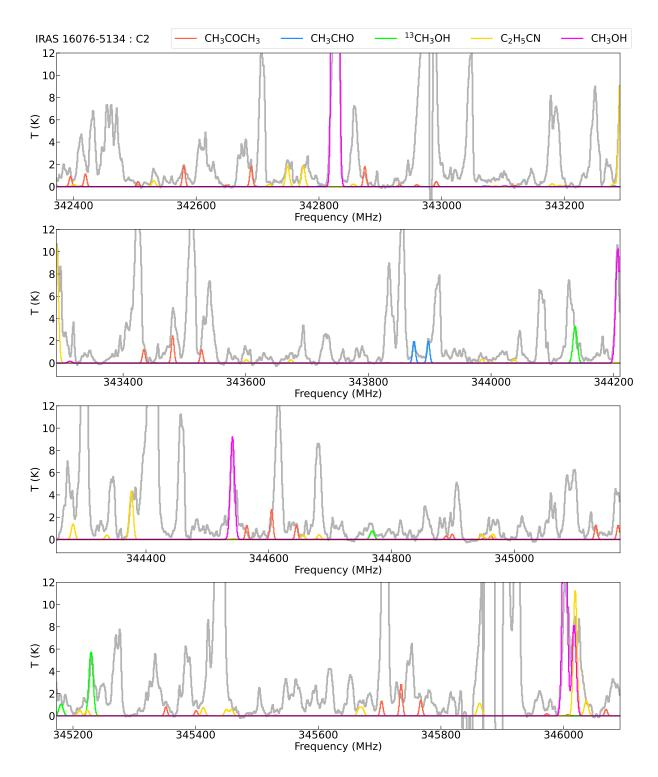


Fig. B.1. Continued.

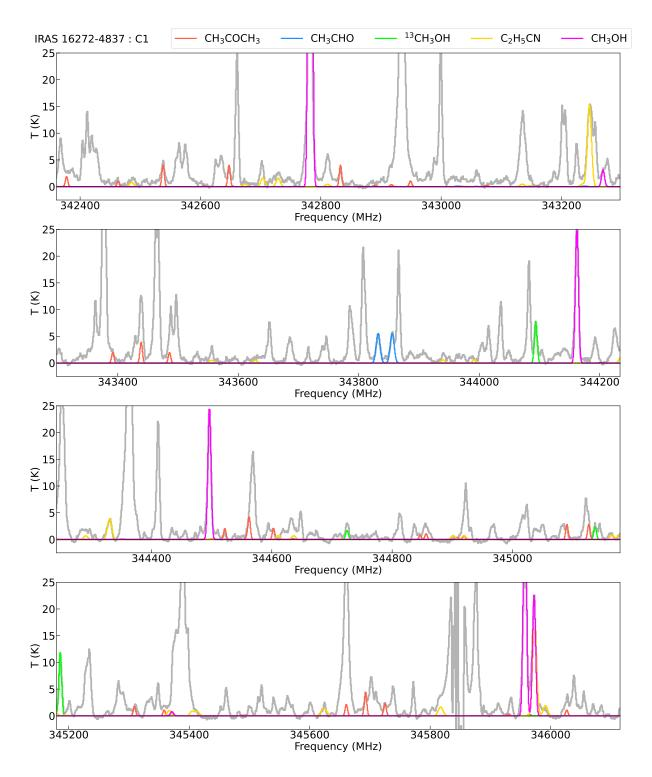


Fig. B.1. Continued.

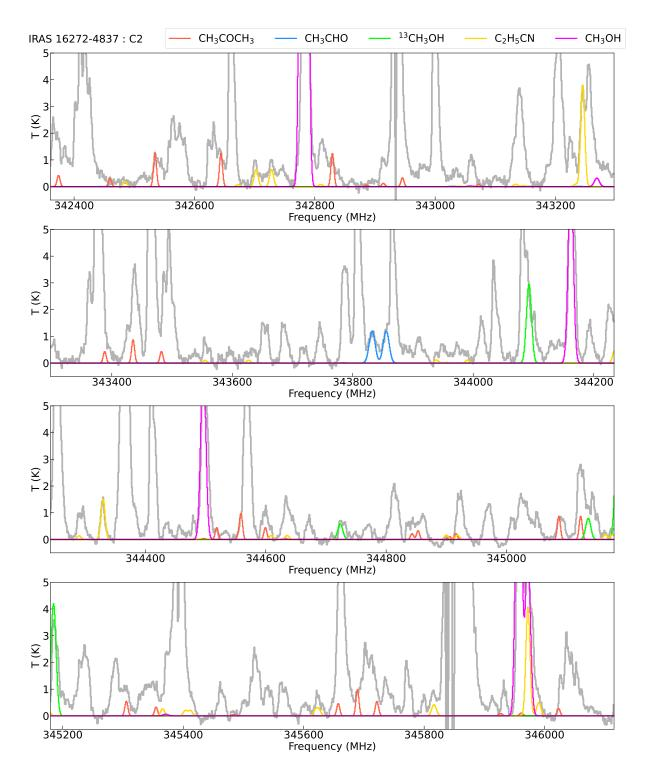


Fig. B.1. Continued.

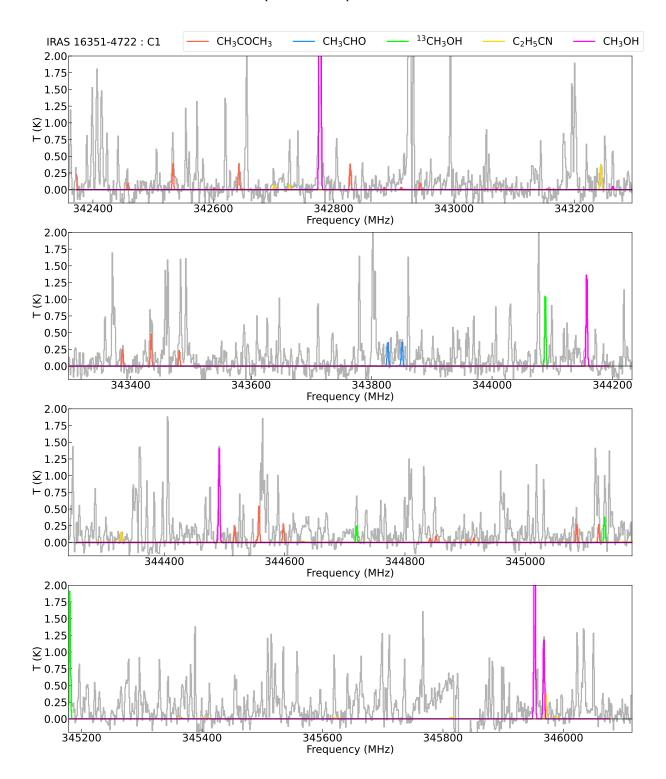


Fig. B.1. Continued.

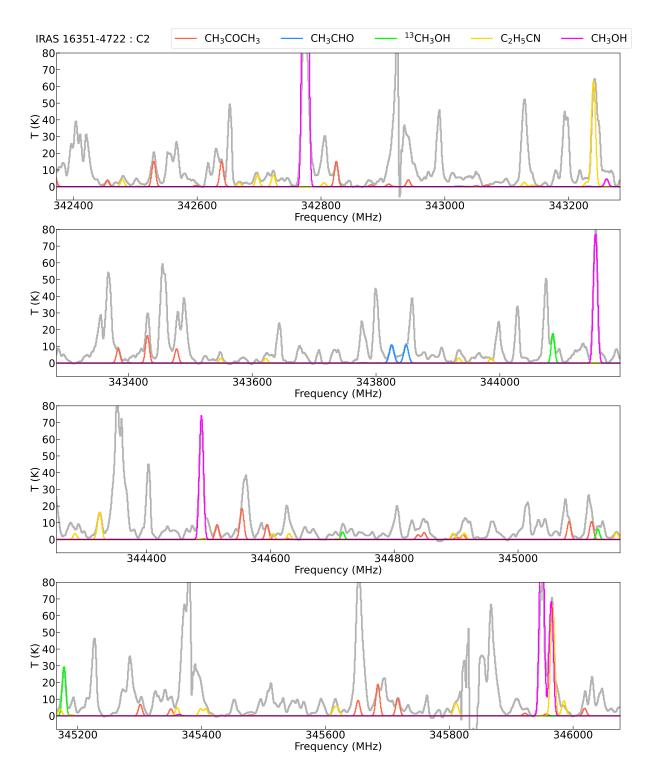


Fig. B.1. Continued.

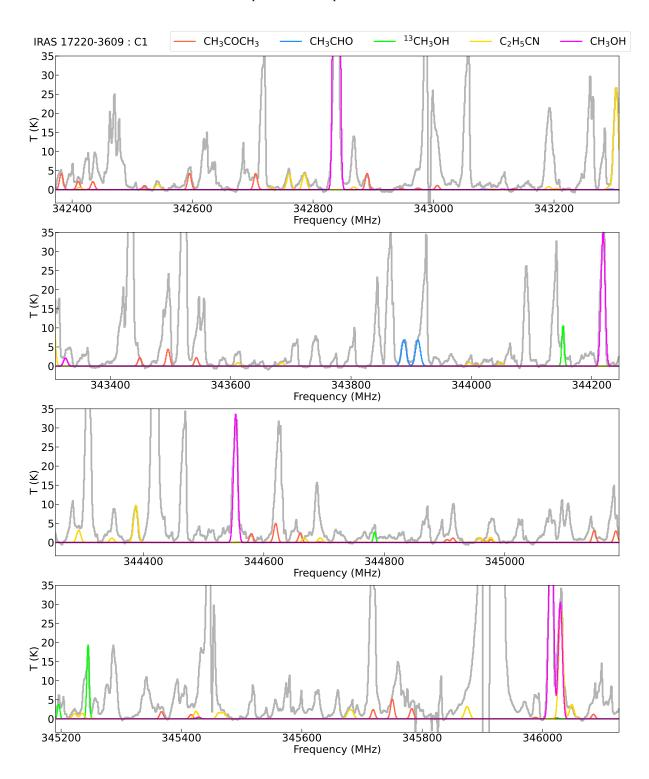


Fig. B.1. Continued.

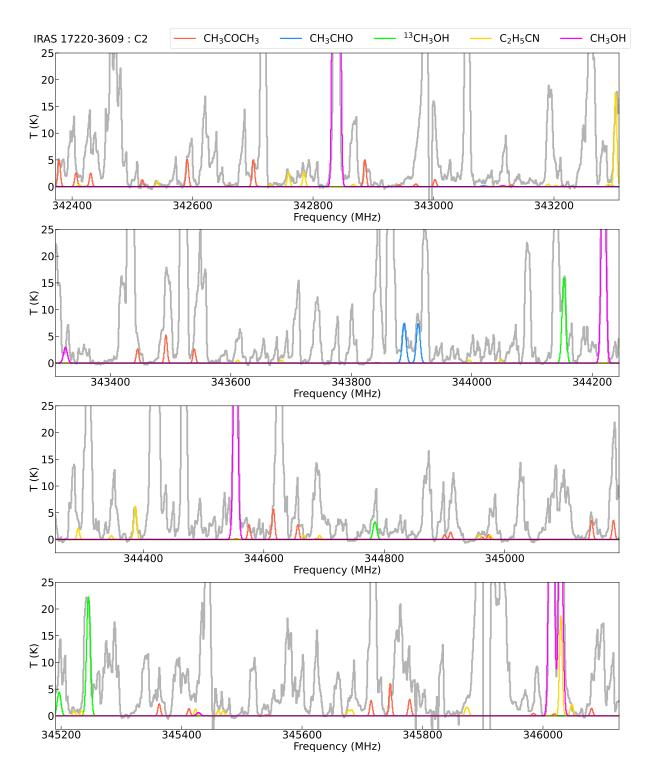


Fig. B.1. Continued.

Appendix C: Molecular transitions

The rotational transitions of the molecules detected in 16 line-rich cores are presented in Table C.1. Molecular parameters for CH_3COCH_3 and CH_3CHO lines are taken from the JPL catalog, while parameters for CH_3OH , $^{13}CH_3OH$, and C_2H_5CN lines are sourced from the CDMS catalog.

Table C.1. Detected spectral transitions of CH₃COCH₃, CH₃CHO, CH₃OH, ¹³CH₃OH, and C₂H₅CN.

Frequency	Transition	$S\mu^2$	E_{up}	Note
(MHz)	CH COCH	(D^2)	(K)	
-	CH ₃ COCH ₃ ;v=			
342324.944	30(6,25)-29(5,24) AA	2018.37	282.73	1
342324.944	30(5,25)-29(6,24) AA	1211.16	282.73	1
342410.641	17(17,1)-16(16,1) EA	552.43	146.85	*
342485.234	17(17,0)-16(16,0) EE	2209.99	147.06	*
342553.854	42(3,39)–42(2,40) EE	456.49	484.93	
342553.854	42(4,39)–42(3,40) EE	456.49	484.93	
342594.888 342780.035	17(17,1)–16(16,1) EE 17(17,1)–16(16,0) AA	2210.27 828.92	146.95 147.05	
342780.033	17(17,1)=10(10,0) AA 17(17,0)=16(16,1) AA	1381.37	147.05	
342836.912	18(12,6)–17(11,7) AE	68.59	141.3	2
342864.593	18(12,6)–17(11,7) AA	208.58	141.24	2 3
342896.394	18(12,6)–17(11,7) EE	548.97	141.27	3
343023.152	18(12,6)–17(11,7) EA	133.9	141.31	2
343338.876	31(4,27)-30(5,26) EA	881.62	288.66	4
343338.876	31(5,27)-30(4,26) EA	881.62	288.66	4
343338.918	31(5,27) – 30(4,26) AE	1322.45	288.66	4
343338.918	31(4,27)-30(4,26) AE	440.84	288.66	4
343386.006	31(4,27) – 30(4,26) EE	3176.31	288.63	5
343386.006	31(5,27)-30(5,26) EE	3176.31	288.63	5
343386.006	31(4,27)-30(5,26) EE	349.64	288.63	5 5
343386.006	31(5,27)-30(4,26) EE	349.64	288.63	5
343433.081	31(4,27)-30(5,26) AA	2203.26	288.61	6
343433.081	31(5,27)-30(4,26) AA	1322.11	288.61	6
344468.948	32(4,29)–31(3,28) EA	955.83	293.77	Ü
344468.948	32(3,29)-31(4,28) EA	955.83	293.77	
344468.985	32(3,29)–31(3,28) AE	1433.77	293.77	
344468.985	32(4,29)-31(4,28) AE	477.95	293.77	
344505.598	16(9,7)–15(8,8) EE	183.87	109.49	7
344509.424	32(4,29)-31(3,28) EE	3469.95	293.73	7
344509.424	32(4,29)-31(4,28) EE	353.28	293.73	7
344509.424	32(3,29)-31(3,28) EE	353.28	293.73	7
344509.424	32(3,29)-31(4,28) EE	3469.95	293.73	7
344549.874	32(4,29)-31(3,28) AA	2389.27	293.69	
344549.874	32(3,29)-31(4,28) AA	1433.73	293.69	
344793.57	18(15,3)-17(14,3) EA	397.32	150.91	8
344803.465	18(15,4)-17(14,3) AE	595.35	150.81	8
344855.635	18(15,3)-17(14,4) AE	198.44	150.81	
344866.506	18(15,4)-17(14,4) EA	396.52	150.71	9
345037.5	18(15,3)-17(14,3) EE	1589.87	150.87	10
345073.724	18(15,4)-17(14,4) EE	1588.26	150.77	6
345256.037	18(15,4)-17(14,3) AA	994.36	150.83	
345305.365	18(15,3)–17(14,4) AA	596.65	150.83	1
345607.709	33(2,31)-32(2,30) EA	1030.69	298.09	11
345607.709	33(3,31)-32(3,30) EA	1030.69	298.09	11
345607.736	33(3,31)-32(3,30) AE	1545.71	298.09	11
345607.736	33(2,31)-32(2,30) AE	515.26	298.09	11
345639.619	33(3,31)-32(3,30) EE	3529.95	298.03	
345639.619	33(3,31)-32(2,30) EE	592.06	298.03	
345639.619	33(2,31)-32(2,30) EE	3529.95	298.03	
345639.619	33(2,31)-32(3,30) EE	592.06	298.03	
345671.524	33(2,31)-32(2,30) AA	1545.65	297.98	1
345671.524	33(3,31)-32(3,30) AA	2575.79	297.98	1
345673.954	15(7,8)-14(6,9) EE	115.74	92.94	1
345875.586	24(12,12)-23(13,11) AE	152.92	235.24	12
345877.896	24(12,12)-23(13,11) EA	305.88	235.24	12
345912.434	15(7,8)-14(6,9) AA	72.39	92.88	13
345973.657	24(12,12)–23(13,11) EE	1221.85	235.24	6

Table C.1. Continued.

Frequency (MHz)	Transition	$S\mu^2$ (D ²)	E _{up} (K)	Note
	CH ₃ CHO;v=	=0		
343779.382	18(2,17)-17(2,16) E	224.63	166.47	*
343802.725	18(2,17)-17(2,16) A	224.54	166.46	1
	CH ₃ OH;v=	0		
342729.796	13(1,12)-13(0,13) A	97.52	227.47	*
344109.039	18(2,17)–17(3,15) E	21.24	419.40	1
344443.433	19(1,19)–18(2,16) A	23.97	451.23	-
345903.916	16(1,15)–15(2,14) A	28.52	332.65	
345919.260	18(3,15)-17(4,14) E	22.41	459.43	2
	¹³ CH ₃ OH;v=	=0		
344040.629	8(3,6)-9(2,8)	2.17	144.49	
344671.733	3(3,0)-4(2,2)	0.25	61.55	1
345083.793	2(2,0)-3(1,3)	0.30	44.60	_
345132.599	4(0,4)-3(1,3)	1.55	35.76	
	$C_2H_5CN;v=$:0		
342433.950	40(2,38)-39(3,37)	30.09	360.89	1
342651.886	15(5,11)-14(4,10)	9.20	79.39	•
342677.561	15(5,10)-14(4,11)	9.20	79.39	
343194.574	38(5,33)-37(5,32)	553.54	347.41	*
343503.727	41(8,33)-41(7,34)	32.96	441.47	2
343576.364	41(8,34)-41(7,35)	32.96	441.47	3
343888.020	40(8,32)-40(7,33)	32.01	423.82	4
343940.188	40(8,33)-40(7,34)	32.01	423.82	2
344238.762	39(8,31)-39(7,32)	31.06	406.61	4
344275.871	39(8,32)-39(7,33)	31.06	406.61	
344278.941	10(6,4)-9(5,5)	8.98	63.67	
344278.941	10(6,5) - 9(5,4)	8.98	63.67	
344558.366	38(8,30)-38(7,31)	30.11	389.82	
344584.505	38(8,31)-38(7,32)	30.12	389.82	2
344849.257	37(8,29) - 37(7,30)	29.18	373.47	
344867.347	37(8,30)-37(7,31)	29.18	373.47	5
345113.287	36(8,28) - 36(7,29)	28.25	357.55	
345125.723	36(8,29)-36(7,30)	28.25	357.55	
345314.812	36(3,34)-35(2,33)	23.96	295.89	2
345352.535	35(8,27)-35(7,28)	27.33	342.06	
345361.010	35(8,28)-35(7,29)	27.32	342.06	_
345568.673	34(8,26)-34(7,27)	26.40	327.00	3
345574.337	34(8,27)-34(7,28)	26.41	327.00	3
345763.372	33(8,25)-33(7,26)	25.49	312.37	
345767.098	33(8,26)-33(7,27)	25.49	312.37	
345921.198	39(3,37)-38(3,36)	573.72	344.46	6
345938.020	32(8,24)-32(7,25)	24.58	298.17	
345940.515	32(8,25)-32(7,26)	24.58	298.17	

Notes. $S\mu^2$ is the product of the line strength (S) and the square of the dipole moment (μ). E_{up} represents the upper level energy. Asterisks mark the transitions of the molecules that are used for Fig. 2.

 CH_3COCH_3 transitions: (1) blended with $^{34}SO_2$ transition lines; (2) blended with unidentified molecular lines; (3) blended with CS transition lines; (4) blended with H_2CS transition lines; (5) blended with H_2CCO transition lines; (6) blended with CH_3COCHO transition lines; (7) blended with CH_3COCH_3 transition lines; (8) blended with CH_2COCH_3 transition lines; (9) blended with CH_2COCH_3 transition lines; (10) blended with CH_3COCH_3 transition lines; (11) blended with $CCCCH_3$ transition lines; (12) blended with CL_3COCH_3 transition lines; (13) blended with CL_3COCH_3 transition lines; (14) blended with CL_3COCH_3 transition lines; (15) blended with CL_3COCH_3 transition lines; (16) blended with CL_3COCH_3 transition lines; (17) blended with CL_3COCH_3 transition lines; (18) blended with CL_3COCH_3 transition lines; (19) blended with CL_3COCH_3 transition li

CH₃CHO transitions: (1) blended with H₂CS transition lines.

 CH_3OH transitions: (1) blended with CH_3OCHO (v=1) transition lines; (2) blended with C_2H_5CN transition lines. The 13(1,12)-13(0,13)A and 16(1,15)-15(2,14)A transitions of CH_3OH are optically thick.

¹³CH₃OH transitions: (1) blended with CH₃OCHO transition lines.

 C_2H_5CN transitions: (1) blended with CH_2DOH transition lines; (2) blended with unidentified molecular lines; (3) blended with CH_3OCHO (v=1) transition lines; (4) blended with CH_3OCHO transition lines; (5) blended with CH_2DOH and CH_3COCH_3 transition lines; (6) blended with CH_3OH transition lines.